Acta Crystallographica Section D
Biological Crystallography
ISSN 0907-4449

The TLR signalling adaptor TRIF/TICAM-1 has an N-terminal helical domain with structural similarity to IFIT proteins

M. Obayed Ullah,[a,b,c]*‡ Thomas Ve,[a,b,c]‡ Matthew Mangan,[d] Mohammed Alaidarous,[a,b,c] Matthew J. Sweet,[b,c] Ashley Mansell[d] and Bostjan Kobe[a,b,c]*

[a]School of Chemistry and Molecular Biosciences, University of Queensland, Brisbane, Queensland 4072, Australia, [b]Institute for Molecular Bioscience, University of Queensland, Brisbane, Queensland 4072, Australia, [c]Australian Infectious Diseases Research Centre, University of Queensland, Brisbane, Queensland 4072, Australia, and [d]Centre for Innate Immunity and Infectious Diseases, Monash Institute of Medical Research, Monash University, Melbourne, Victoria 3168, Australia

‡ These authors contributed equally to this work.

Correspondence e-mail: obayed.ullah@uqconnect.edu.au, b.kobe@uq.edu.au

© 2013 International Union of Crystallography
Printed in Singapore – all rights reserved

Received 12 June 2013
Accepted 9 August 2013

PDB References:
TRIF-NTD$^{A66M/L113M}$, 4bsx; wild-type TRIF-NTD, 4c0m

TRIF/TICAM-1 (TIR domain-containing adaptor inducing interferon-β/TIR domain-containing adaptor molecule 1) is the adaptor protein in the Toll-like receptor (TLR) 3 and 4 signalling pathway that leads to the production of type 1 interferons and cytokines. The signalling involves TIR (Toll/interleukin-1 receptor) domain-dependent TRIF oligomerization. A protease-resistant N-terminal region is believed to be involved in self-regulation of TRIF by interacting with its TIR domain. Here, the structural and functional characterization of the N-terminal domain of TRIF (TRIF-NTD) comprising residues 1–153 is reported. The 2.22 Å resolution crystal structure was solved by single-wavelength anomalous diffraction (SAD) using selenomethionine-labelled crystals of TRIF-NTD containing two additional introduced Met residues (TRIF-NTD$^{A66M/L113M}$). The structure consists of eight antiparallel helices that can be divided into two subdomains, and the overall fold shares similarity to the interferon-induced protein with tetratricopeptide repeats (IFIT) family of proteins, which are involved in both the recognition of viral RNA and modulation of innate immune signalling. Analysis of TRIF-NTD surface features and the mapping of sequence conservation onto the structure suggest several possible binding sites involved in either TRIF auto-regulation or interaction with other signalling molecules or ligands. TRIF-NTD suppresses TRIF-mediated activation of the interferon-β promoter, as well as NF-κB-dependent reporter-gene activity. These findings thus identify opportunities for the selective targeting of TLR3- and TLR4-mediated inflammation.

1. Introduction

The innate immune system constitutes the first line of defence against microbial infection or endogenous danger signals. Pathogen-associated or danger-associated molecular patterns (PAMPs/DAMPs) are recognized by pattern-recognition receptors (PRRs) such as the membrane-bound Toll-like and C-type lectin receptors (TLRs and CLRs) or the cytosolic NOD-like and RIG-I-like receptors (NLRs and RLRs) (Bonardi *et al.*, 2012; Eisenächer & Krug, 2012; Kawai & Akira, 2010; Kingeter & Lin, 2012). After PAMP/DAMP recognition, these receptors recruit specific adaptor proteins that determine the specificity of inflammatory response *via* the activation of distinct transcription factors and pro-inflammatory genes (Werts *et al.*, 2006; Ve *et al.*, 2012).

TLRs are the best-characterized members of the PRR family and recognize PAMPs such as lipopolysaccharides, lipopeptides or bacterial flagellin at the surface of immune

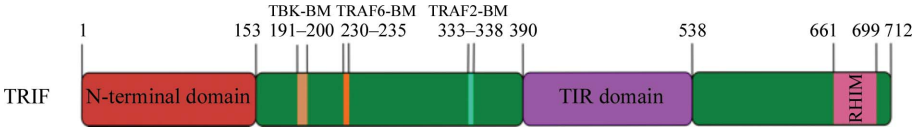

Figure 1
Schematic representation of the primary structure of TRIF, highlighting structural and functional motifs. TRIF-NTD (TRIF N-terminal domain) is a globular domain consisting of eight helices (this work). TBK1-BM (TANK-binding kinase 1 binding motif) corresponds to residues 191–200 (Tatematsu *et al.*, 2010). TRAF6-BM (TRAF6-binding motif) and TRAF2-BM (TRAF2-binding motif) correspond to residues 230–235 and 333–338, respectively (Sasai *et al.*, 2010). Residues 390–538 are predicted to correspond to a TIR domain. An RHIM (receptor-interacting protein homotypic interaction motif) is found in the C-terminal region of TRIF (Meylan *et al.*, 2004).

cells, while viral or microbial nucleic acids are recognized by endosomally localized TLRs (Barton & Kagan, 2009). TLRs contain a PAMP-recognizing leucine-rich repeat (LRR) domain, a transmembrane helix and a cytosolic TIR (Toll/interleukin-1 receptor) domain involved in TIR–TIR domain interactions. PAMP binding leads to oligomerization of TLRs and consequently their TIR domains, which facilitates the recruitment of cytosolic TIR domain-containing adaptor proteins and signalling. The selective recruitment of one or several adaptors to specific TLRs triggers the activation of distinct signalling pathways (O'Neill & Bowie, 2007; Akira *et al.*, 2006; Ve *et al.*, 2012). TRIF/TICAM-1 (TIR domain-containing adaptor inducing interferon-β/TIR domain-containing adaptor molecule 1) is directly recruited to TLR3, while association with TLR4 requires the TIR domain-containing bridging adaptor TRAM/TICAM-2 (TRIF-related adaptor molecule/TIR domain-containing adaptor molecule 2). TRIF orchestrates a signalling response characterized by the inducible expression of interferon-β (IFNβ) and IFNβ-dependent genes *via* the activation of the transcriptional factors IRF-3, NF-κB and AP-1 (Oshiumi, Matsumoto *et al.*, 2003; Yamamoto *et al.*, 2003; Fitzgerald *et al.*, 2003; Oshiumi, Sasai *et al.*, 2003).

In the cytoplasm of resting cells, TRIF is expressed at a low level in a diffuse form (Oshiumi, Matsumoto *et al.*, 2003; Funami *et al.*, 2007), while in poly(I:C)-stimulated cells TRIF first transiently associates with TLR3 and subsequently (after dissociation from the receptor) forms speckle-like structures that also contain downstream signalling molecules (Funami *et al.*, 2007; Tatematsu *et al.*, 2010). Human TRIF (712 amino acids) consists of an N-terminal protease-resistant domain with a predicted helical structure followed by a proline-rich unstructured region containing TBK1 (TANK-binding kinase) and TRAF6 (tumour necrosis factor receptor-associated factor 6) binding motifs, a central TIR domain and a C-terminal region containing an RIP homotypic interaction motif (RHIM) (Fig. 1). Both the TIR and the RHIM domains are required for TRIF homo-oligomerization (Funami *et al.*, 2008). The TIR domain also facilitates the direct interaction with TLR3 and TRAM through TIR–TIR domain interactions, while heterotypic RHIM–RHIM domain interactions enable TRIF to associate with the death domain-containing kinases RIP1 and RIP3, leading to NF-κB activation and cell death (Meylan *et al.*, 2004; Han *et al.*, 2004; Kaiser & Offermann, 2005; He *et al.*, 2011). Recruitment of TRAF6 also results in NF-κB activation (Sasai *et al.*, 2010), while binding of TBK1 leads to IRF-3 activation and IFNβ induction (Tatematsu *et al.*, 2010; Han *et al.*, 2010). Several regulatory molecules [for example, members of the tripartite motif (TRIM) family of proteins] further regulate the signalling either positively or negatively to maintain a balanced response, as both over-activation and underactivation of TRIF-mediated signalling have undesirable effects. The molecular mechanisms of the interaction of TRIF with its binding partners are unknown.

A deletion mutant of TRIF lacking the N-terminal protease-resistant domain (residues 1–176) has a higher ability for IFNβ promoter activation compared with wild-type TRIF and forms speckle-like structures in resting cells (Tatematsu *et al.*, 2010). Immunoprecipitation and protein-fragment complementation analyses have shown that the TRIF N-terminal domain interacts with the TIR domain, which suggests that it can fold back onto the TIR domain in the resting state of TRIF, and acts as a negative regulator preventing downstream signalling molecules such as TBK1, RIP1/3 and TRAF6 from accessing their binding sites.

To understand the molecular basis of TRIF auto-regulation, we solved the crystal structure of the N-terminal domain of TRIF (TRIF-NTD) at 2.22 Å resolution. The structure contains eight antiparallel α-helices that can be divided into two subdomains by a long linker region. The overall fold of TRIF-NTD shares significant structural similarity to the IFN-induced protein with tetratricopeptide repeats (IFIT) family of proteins, which have been shown to bind viral RNA and to regulate innate immune responses by modulating interactions between components in the type 1 IFN signalling pathway. Analysis of the structure reveals specific surface regions that could be involved in TRIF auto-regulation or interact with other signalling molecules or ligands. Reporter assays in transfected cells show that TRIF-NTD suppresses TRIF-mediated induction of both the IFNβ promoter and an NF-κB-dependent promoter, and could therefore serve as an experimental tool and therapeutic reagent for targeting TLR3- and TLR4-mediated inflammation.

2. Materials and methods

2.1. Structure determination and refinement

Details of the expression, purification and X-ray diffraction data collection of TRIF-NTD have been reported previously (Ullah *et al.*, 2013). In brief, we crystallized the N-terminal protein fragment of TRIF encoding residues 1–153 (TRIF-NTD). The structure was solved by single-wavelength anomalous diffraction (SAD) using selenomethionine-labelled crystals of TRIF-NTD containing two additional Met residues (TRIF-NTD$^{A66M/L113M}$). X-ray diffraction data sets were collected at two wavelengths [1.1070 Å (high-resolution data

set) and 0.9793 Å (Se peak data set)] and the resolution limits of the data sets corresponded to 2.22 and 2.48 Å, respectively. The data for the high-resolution data set could not be used to a resolution higher than 2.22 Å because of a rapid drop in data completeness owing to the geometry of data collection. The crystals had the symmetry of space group *P*1 with four molecules in the asymmetric unit. SAD phasing was performed using the Se peak data set and the program *AutoSol* in the *PHENIX* suite (Adams *et al.*, 2013). The initial model was built into the resulting density using *ARP/wARP* (Langer *et al.*, 2008) and several cycles of refinement were performed using *phenix.refine* in the *PHENIX* suite with model building using *Coot* (Emsley *et al.*, 2010) using the high-resolution data set. Programs from the *CCP*4 suite (Winn *et al.*, 2011) were also used at different stages of structure determination. Crystals of wild-type TRIF-NTD diffracted X-rays to resolutions between 1.9 and 2.8 Å. The data from these crystals were originally processed in space group $P2_12_12_1$, with unit-cell parameters a = 48.02, b = 77.18, c = 85.15 Å (Ullah *et al.*, 2013), and although a molecular-replacement solution could be found using *Phaser* (McCoy *et al.*, 2007) with the TRIF-NTD$^{A66M/L113M}$ structure as a template, the model could not be refined (R_{work} > 44% and R_{free} > 48%). However, the data from one of the TRIF NTD crystals that diffracted X-rays to 2.8 Å resolution could also be processed in space group *P*1 with a similar unit cell to TRIF-NTD$^{A66M/L113M}$. This structure was solved using molecular replacement and refined using *BUSTER-TNT* (Blanc *et al.*, 2004) to final R_{work} and R_{free} values of 25.2 and 29.1%, respectively. Comparison of the packing of the molecules in the crystals of the $P2_12_12_1$ symmetry wild-type TRIF-NTD, based on the possible molecular-replacement solution, with those in the crystals of the *P*1 symmetry TRIF-NTD and TRIF-NTD $^{A66M/L113M}$ revealed a related but not identical arrangement of molecules. We suggest that the packing of molecules in the crystals deviates slightly from an arrangement that would be compatible with higher (space group $P2_12_12_1$) crystallographic symmetry (*i.e.* such that the symmetry axes relating the molecules could be propagated in the crystal as crystallographic symmetry). *PyMOL* (http://www.pymol.org) and *Pro-origami* (Stivala *et al.*, 2011) were used to generate the figures. Coordinates and structure factors for TRIF-NTD$^{A66M/L113M}$ and wild-type TRIF-NTD have been deposited in the Protein Data Bank as entries 4bsx and 4c0m, respectively.

2.2. Analysis of the structure

The structure was compared with available structures using *DALI* (Holm & Rosenström, 2010). The electrostatic potential was mapped onto the surface using *APBS* (Unni *et al.*, 2011). Multiple sequence alignments were performed using *ClustalW* (Larkin *et al.*, 2007) and formatted using *ESPript* (Gouet *et al.*, 2003). Interfaces were analyzed using the *PISA* server (Krissinel & Henrick, 2007); the buried surface areas reported correspond to the total buried surface area contributed by both interacting partners.

2.3. Transient transfection of cells and reporter activity

Human embryonic kidney (HEK) 293 cells were incubated in Dulbecco's modified Eagle's medium supplemented with 10% foetal calf serum, 2 ml glutamine and maintained in a 310 K humidified atmosphere. The cells (2×10^4 ml^{-1}) were seeded in 96-well plates 24 h prior to transfection. Transfections were performed with Fugene 6 (Roche Diagnostics). NF-κB-dependent reporter-gene expression was determined using the 5× κB-luciferase reporter construct (Stratagene) concomitantly with the indicated vectors. The p125-luc luciferase plasmid contains the full-length IFNβ promoter upstream of the firefly luciferase gene and is referred to as the IFNβ-luciferase reporter. The *Renilla* luciferase-thymidine kinase-encoding plasmid (pRL-TK; Promega, Madison, Wisconsin, USA) was used to normalize for transfection efficiency and pEF-BOS empty vector was used to maintain constant amounts of DNA. Cells transfected with pEF-Bos-TRAM, pEF-Bos-TRIF and Flag-tagged TLR3 either in the presence or absence of TRIF-NTD (in a pEF6/V5-His-TOPO vector) were lysed using Passive Lysis Buffer (Promega) and assayed for luciferase and *Renilla* luciferase activity using the *Renilla* Luciferase Assay System reagent (Promega). Luminescence readings were corrected for *Renilla* luciferase activity and expressed as fold increases over nonstimulated control values.

2.4. Biophysical analyses

MALLS (multi-angle laser light scattering) experiments were carried out using a DAWN HELEOS II 18-angle light-scattering detector coupled with an Optilab rEX refractive-index detector (Wyatt Technology) and combined inline with a Superdex 200 10/300 GL (GE Healthcare) size-exclusion column connected to a Prominence UFLC (Shimadzu). The buffer for all experiments corresponded to 10 m*M* HEPES pH 7.5, 150 m*M* NaCl, 2 m*M* DTT. For circular-dichroism (CD) analyses, the protein samples were prepared by dialysis overnight into 10 m*M* phosphate buffer pH 7.5, 100 m*M* NaCl. The concentrations of the proteins were in the range 4–5 μM. The CD spectra were collected using a Jasco J710 spectropolarimeter at 298 K. The measurements were recorded at 0.2 nm wavelength increments from 260 to 195 nm at 20 nm min^{-1} using a 0.1 cm path-length cell, a 1 nm bandwidth, a 1 s response time and five accumulations. After correction for the buffer baseline contribution, the spectra were analyzed using the online programs *CAPITO* (Wiedemann *et al.*, 2013) and *SOMCD* (Unneberg *et al.*, 2001).

3. Results and discussion

3.1. Functional characterization of TRIF-NTD

TRIF-NTD has previously been proposed to form an intramolecular interaction with the TIR domain of TRIF, thus preventing the homodimerization of TRIF and binding to downstream signalling molecules (Tatematsu *et al.*, 2010). We therefore tested whether TRIF-NTD could act functionally as a dominant negative to inhibit TRIF-induced signalling using

the TRIF-NTD construct structurally characterized in this study (TRIF-NTD, comprising residues 1–153). Expression of TRIF-NTD did not activate either the IFNβ or the NF-κB promoter (Supplementary Fig. S1*a*[1]). We first established a dose of TRIF that activated both the NF-κB and IFNβ-luciferase promoters and chose 1 ng of TRIF DNA as a suboptimal activating dose, such that we would observe any inhibition of signalling (Supplementary Fig. S1*b*). Ectopic expression of TRIF-NTD in a 25-fold to 100-fold excess compared with TRIF was able to inhibit both TRIF-mediated IFNβ promoter activation (Fig. 2*a*, left panel) and TRIF-induced NF-κB promoter activity (Fig. 2*a*, right panel).

To provide further support for the observed effects of TRIF-NTD on TRIF-mediated signalling, we demonstrated that TRIF-NTD is able to inhibit TRAM-induced IFNβ or NF-κB promoter activation (left and right panels in Fig. 2*b*, respectively). We also assessed the ability of TRIF-NTD to suppress TLR3-mediated activation of signalling pathways. As can be observed in Fig. 2(*c*), TRIF-NTD noticeably and consistently inhibited the degree of TLR3-induced IFNβ (left panel) and NF-κB (right panel) promoter activation, particularly at higher doses.

Importantly, we were successful in suppressing TRAM-induced activation of the signalling pathway by TRIF-NTD. As TRAM is an upstream activator of TRIF, the ability of TRIF-NTD to suppress signalling implies that excess TRIF-NTD is able to compete with subsequent activation of TRIF to suppress downstream signalling. This therefore suggests that the association between TRIF-NTD and the TIR domain of TRIF is dynamic and could be suppressed through molecular competition if excess TRIF-NTD is available during activation.

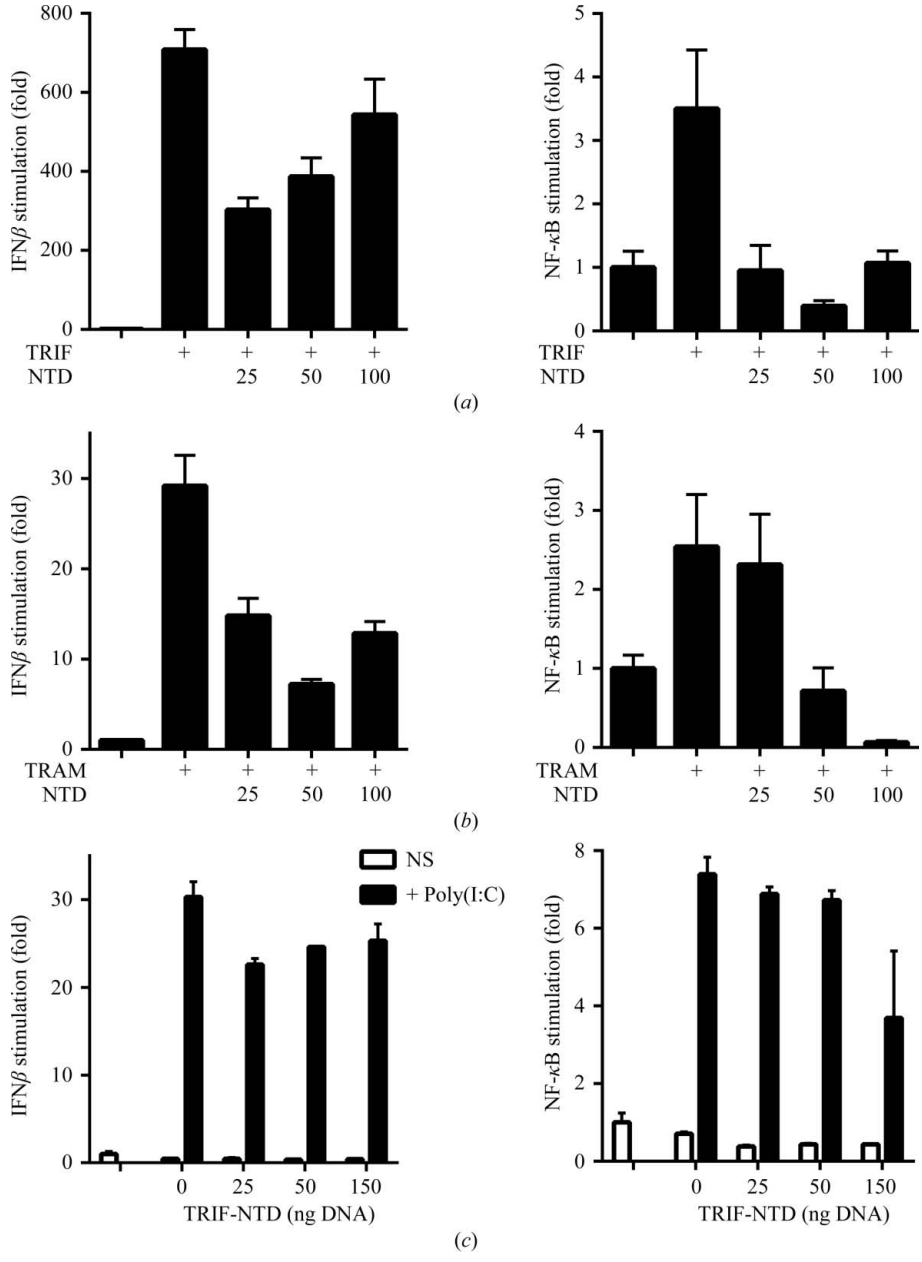

Figure 2
TRIF-NTD inhibits TLR3- and TRIF-mediated activation of the IFNβ promoter and an NF-κB-dependent promoter. (*a*) HEK293 cells (2×10^4 ml^{-1}) were transiently transfected for 24 h with *Renilla* luciferase-thymidine kinase and IFNβ-luciferase (left panel) or NF-κB-luciferase (right panel) in conjunction with TRIF (1 ng) and a dose range of TRIF-NTD (25–100 ng). (*b*) TRAM (25 ng) activity was inhibited in a dose-dependent manner by the addition of TRIF-NTD (25–100 ng) and IFNβ-luciferase (left panel) or NF-κB-luciferase (right panel) evaluated following cell lysis. (*c*) Cells were made responsive to the TLR3 ligand poly(I:C) (10 µg ml^{-1}) by transfection with TLR3 (5 ng) and were inhibited by co-expression with TRIF-NTD in a dose-dependent manner (25–150 ng). Results correspond to the mean ± standard error and are representative of three independent experiments.

Taken together, our results support the theory of Matsumoto and coworkers (Tatematsu *et al.*, 2010) that excess expression of TRIF-NTD acts to suppress the activity of TRIF and modulates the downstream signalling pathways leading to activation of both the IFNβ or NF-κB promoters. These results suggest that therapeutically targeting TRIF-mediated signalling with excess TRIF-NTD could potentially modulate TLR3- or TLR4-mediated signal transduction and inflammation.

[1] Supplementary material has been deposited in the IUCr electronic archive (Reference: CB5041). Services for accessing this material are described at the back of the journal.

3.2. Structure determination of TRIF-NTD

To aid in understanding its function and in any therapeutic application, we set out to structurally characterize TRIF-NTD. Constructs encompassing residues 1–153 and 1–177 of human TRIF were produced in *Escherichia coli* and purified using a combination of IMAC (immobilized metal-ion affinity chromatography) and gel filtration. Both constructs crystallized, but only the shorter construct produced diffraction-quality crystals (Ullah *et al.*, 2013). The N-terminal region of TRIF does not share sequence similarity to any proteins of known structure and only contains two methionine residues. To increase the chances of successful structure determination using SeMet-based experimental phasing, Ala66 and Leu113 were mutagenized to methionine residues (TRIF-NTD$^{A66M/L113M}$). These positions correspond to methionine residues in several mammalian TRIF orthologues (Ullah *et al.*, 2013). The remaining parts of the sequences are highly conserved, suggesting that these mutations should not affect the overall fold of the protein. TRIF-NTD, TRIF-NTD$^{A66M/L113M}$ and TRIF (residues 1–177) are all monomeric in solution (based on MALLS analysis; Supplementary Fig. S2) and have indistinguishable circular-dichroism spectra (Supplementary Fig. S3). SeMet-labelled TRIF-NTD$^{A66M/L113M}$ was successfully purified and yielded plate-like crystals which diffracted X-rays to 2.22 Å resolution. The crystals had the symmetry of the triclinic space group *P*1. An interpretable electron-density map was obtained from an SeMet-labelled derivative using the single-wavelength anomalous diffraction (SAD) technique. The structure was refined to final R_{work} and R_{free} values of 19 and 24%, respectively, with good stereochemistry (Table 1). The final model contains four nearly identical molecules in the asymmetric unit [the maximum root-mean-square distance (r.m.s.d.) for any pair of the molecules was 0.189 Å for all atoms]. The model contains residues 4–148; no electron density was observed for residues 1–3 and 149–153, suggesting that these regions have a disordered or flexible conformation in the crystal. For wild-type TRIF-NTD we have only been able to obtain

Table 1
Structure-solution and refinement statistics.

	TRIF-NTD$^{A66M/L113M}$		
	High-resolution data set	Se peak data set	TRIF-NTD
Data-collection statistics			
Wavelength (Å)	1.1070	0.9793	0.9536
Temperature (K)	100	100	100
Detector	ADSC Quantum 315r CCD	ADSC Quantum 315r CCD	ADSC Quantum 315r CCD
Crystal-to-detector distance (mm)	300.00	399.99	350.00
Rotation range per image (°)	1.0	1.0	1.0
Total rotation range (°)	360	1440	180
Exposure time per image (s)	4.0	1.0	1.0
Space group	*P*1	*P*1	*P*1
Unit-cell parameters			
a (Å)	47.31	47.32	48.0
b (Å)	49.33	49.48	49.4
c (Å)	70.14	70.32	70.9
α (°)	88.66	88.55	88.6
β (°)	77.61	77.63	77.2
γ (°)	72.21	72.26	72.1
Mosaicity (°)	0.22	0.20	1.2
Resolution range (Å)	68.40–2.22 (2.35–2.22)	68.62–2.48 (2.63–2.48)	44.51–2.80 (2.95–2.80)
Total No. of reflections	103753	225375	23984
No. of unique reflections	27104	19519	13337
Completeness (%)	93.7 (71.6)	94.8 (68.9)	89.6 (90.4)
Anomalous completeness (%)	88.1 (63.9)	93.2 (60.0)	
Multiplicity	3.8	11.6	1.8
Anomalous multiplicity	2.0	5.8	
$\langle I/\sigma(I)\rangle$	10.6 (3.7)	17.1 (4.5)	3.9 (2.0)
R_{meas}† (%)	12.0 (43.2)	14.7 (61.4)	20.4 (39.5)
$R_{p.i.m.}$‡ (%)	6.1 (22.7)	4.3 (18.8)	14.4 (27.9)
Overall *B* factor from Wilson plot (Å^2)	23.5	21.4	9.0
Phasing statistics (*AutoSolve*)			
No. of sites (found/all)		11/16	
Figure of merit§		0.38	
Overall score (BAYES-CC¶ × 100)		42.32 ± 9.78	
R factor (after density modification)		0.26	
SKEW††		0.11	
$CORR_{RMS}$‡‡		0.75	
Refinement statistics			
Resolution range (Å)	47.10–2.22		39.70–2.80
No. of reflections, work set	23845		13335
No. of reflections, test set	1877		680
R_{work}§§ (%)	19.01		25.2
R_{free}¶¶ (%)	23.90		29.1
No. of non-H atoms			
Total	4775		4352
Non-solvent	4487		4352
Water	288		0
Average isotropic *B* value (Å^2)	22.6		22.7
R.m.s.d. from ideal geometry			
Bond lengths (Å)	0.014		0.010
Bond angles (°)	1.354		0.970
Ramachadran plot, residues in (%)			
Favoured regions	98.94		96.76
Additionally allowed regions	0.88		3.34
Outlier regions	0.18		0.00

† $R_{meas} = \sum_{hkl}\{N(hkl)/[N(hkl)-1]\}^{1/2}\sum_i |I_i(hkl) - \langle I(hkl)\rangle|/\sum_{hkl}\sum_i I_i(hkl)$, where $I_i(hkl)$ is the *i*th measurement of the intensity of reflection *khl*, $\langle I(hkl)\rangle$ is the mean intensity of reflection *hkl* and $N(hkl)$ is the number of observations of intensity $I(hkl)$ (the multiplicity). ‡ $R_{p.i.m.} = \sum_{hkl}\{1/[N(hkl)-1]\}^{1/2}\sum_i |I_i(hkl) - \langle I(hkl)\rangle|/\sum_{hkl}\sum_i I_i(hkl)$. § An estimate of phase quality and an indicator of the internal consistency of a solution, ranging from 0 to 1. ¶ The Bayesian correlation coefficient score. Bayesian estimates of the quality of experimental electron-density maps are obtained using data from a set of previously solved data sets. †† Skew of the electron density in the map. ‡‡ The correlation of local r.m.s density. §§ $R_{work} = \sum_{hkl}||F_{obs}| - |F_{calc}||/\sum_{hkl}|F_{obs}|$, where F_{obs} and F_{calc} are the observed and calculated structure factors, respectively. ¶¶ R_{free} is equivalent to R_{work} but was calculated using a randomly selected 7.3% of the reflections, which were excluded from all stages of refinement.

diffraction data to 2.8 Å resolution (Table 1). Importantly, there are no significant differences between the structures of wild-type TRIF-NTD and TRIF-NTD$^{A66M/L113M}$ (r.m.s.d. of 0.32 Å for all four chains in the asymmetric unit; Supplementary Fig. S4); we will therefore use the higher resolution structure of TRIF-NTD$^{A66M/L113M}$ for all structural analyses in this paper unless stated otherwise. Representative electron-density maps are shown in Supplementary Fig. S5.

3.3. Overall structure of TRIF-NTD

The crystal structure of TRIF-NTD consists of eight α-helices (α1–α8) connected by loop regions (Figs. 3*a*, 3*b* and 3*c*). The structure can be divided into three parts: the N-terminal 79 residues form an antiparallel five-helix structure and residues 92–148 form an antiparallel three-helix bundle, while residues 80–91 form a long linker loop connecting the two subdomains. Although the linker region separates the two subdomains, they form extensive interactions with each other, as indicated by the buried surface area of about 1520 Å^2. These interactions involve both hydrophobic and polar residues, contributed predominantly by helices α1–α3 in the first subdomain and helices α7–α8 in the second subdomain. Several of these residues are conserved in TRIF variants from mammals, fish and birds (Fig. 4). One distinct interface was observed between two molecules in the TRIF-NTD crystals, yielding a dimeric structure with overall dimensions of 72 × 44 × 38 Å and a buried surface area of approximately 1700 Å^2 (Supplementary Fig. S6). However, analysis of the interface using *PISA* (Krissinel & Henrick, 2007) revealed very few specific side-chain interactions, suggesting that the interface is likely to correspond to a nonspecific crystal-packing interface, which is consistent with MALLS (multi-angle laser light scattering) data showing that TRIF-NTD exists as a monomer in solution (Supplementary Fig. S1; Ullah *et al.*, 2013). Examination of the electrostatic surface potential of TRIF-NTD revealed that the charge is distributed unevenly, with the surface areas contributed by the α3–α5 and α7–α8 helices and the long loop connecting the α5 and α6 helices having an overall electronegative charge, while the face of the molecule contributed by the α2 helix and the tip of the α6 helix is positively charged (Fig. 5).

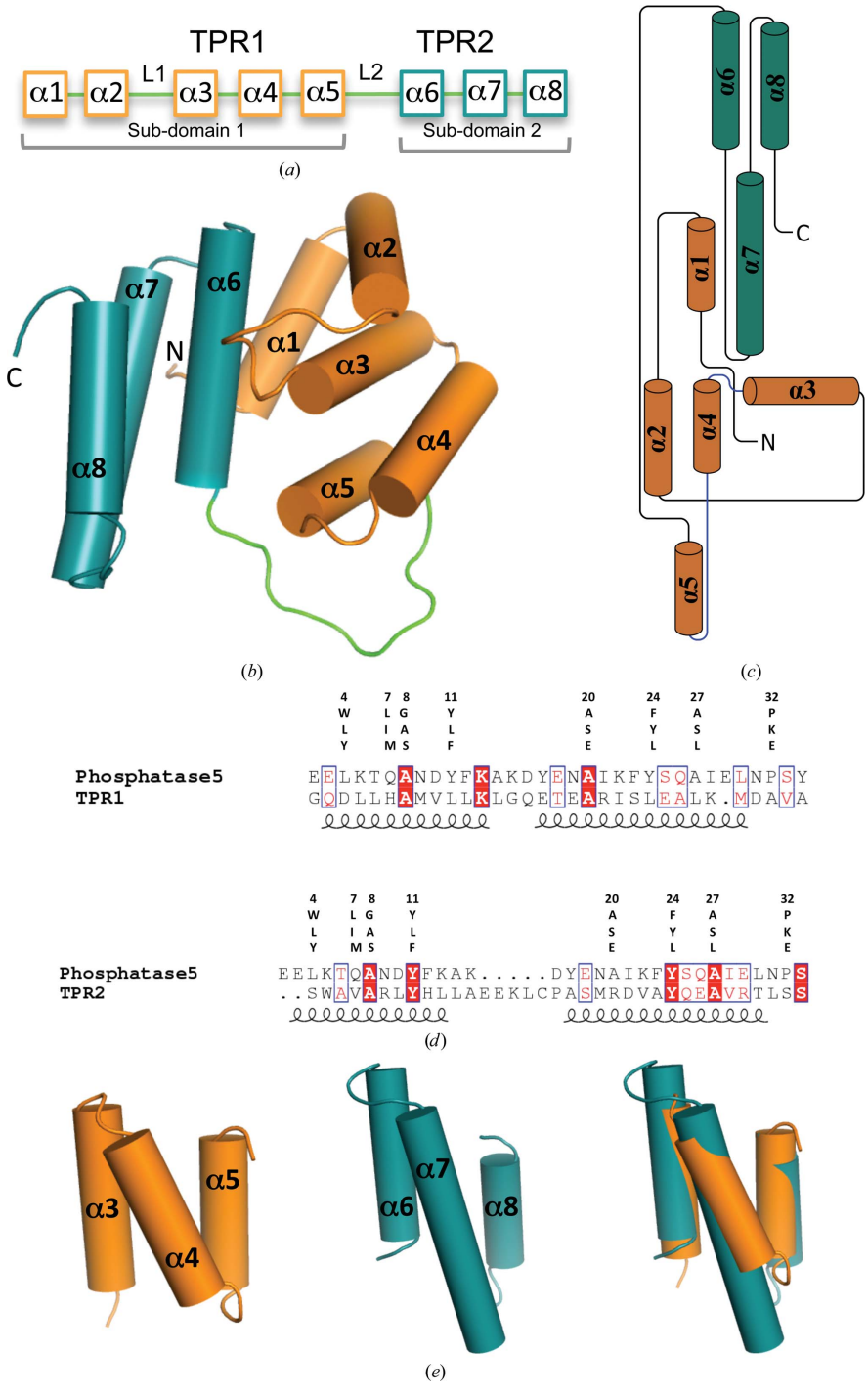

Figure 3
Crystal structure of TRIF-NTD. (*a*) Secondary structure, TPR-like motif features and subdomain organization of TRIF-NTD. (*b*) Cylinder representation of the TRIF-NTD structure. The helices are labelled α1–α8. Subdomains 1 and 2 are highlighted in orange and teal, respectively, while the loop connecting the subdomains is displayed in green. (*c*) Cartoon representation of TRIF-NTD created by the program *Pro-origami* (Stivala *et al.*, 2011). (*d*) Structural alignment of TRIF-NTD TPR-like motifs with typical TPR motifs (TPR1 in phosphatase 5; PDB entry 1a17; Das *et al.*, 1998). The consensus TPR motifs are displayed above the alignments. (*e*) Superimposition of helices α3–α5 (orange) with helices α6–α8 (teal).

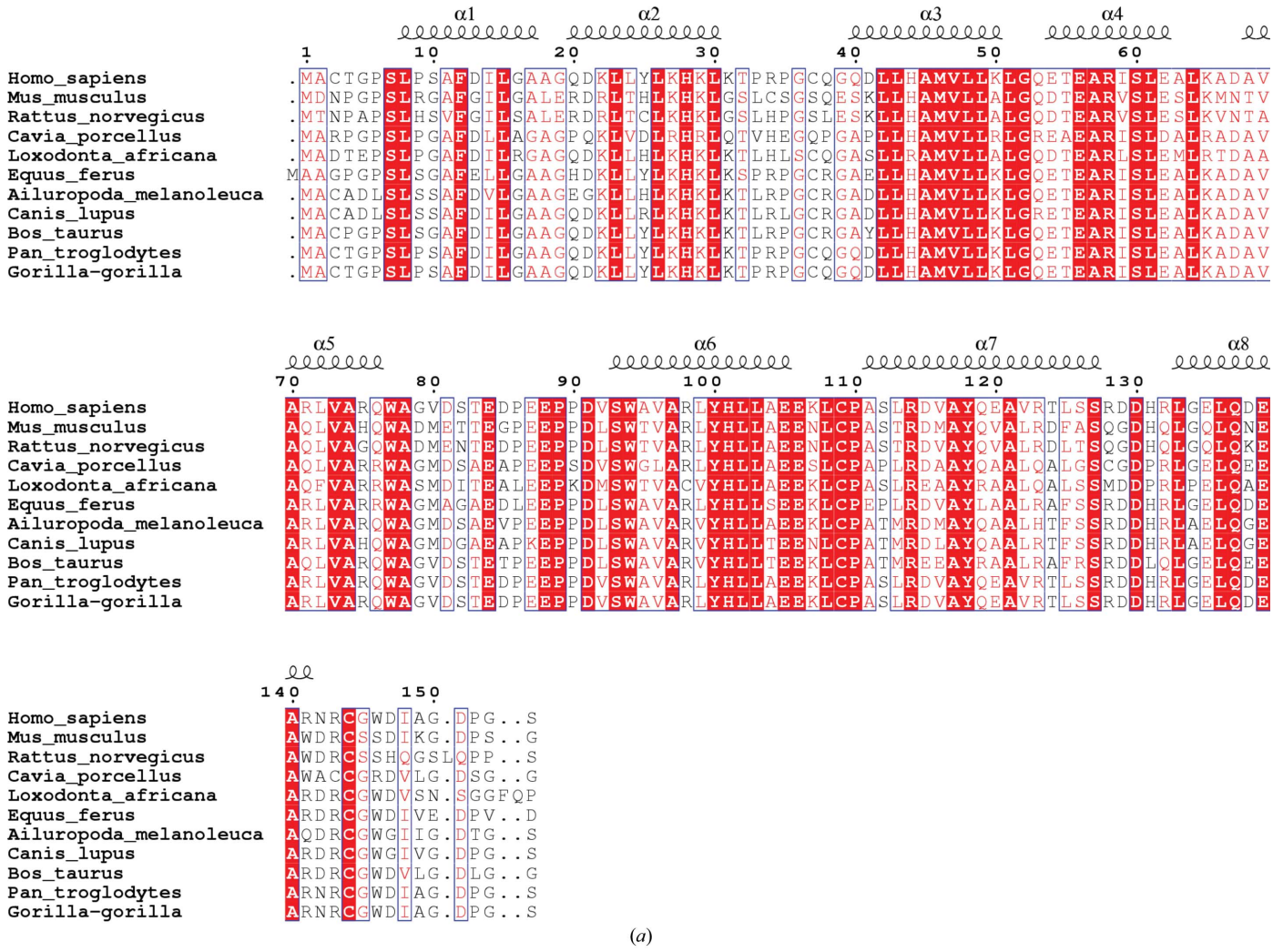

Figure 4
Multiple sequence alignment of TRIF orthologues. Amino-acid sequences were aligned using *ClustalW* (Larkin *et al.*, 2007). The positions of the elements of secondary structure in TRIF-NTD are shown at the top. The alignment was formatted using *ESPript* (Gouet *et al.*, 2003). Strictly conserved residues are indicated in white letters on a red background, while similar residues are indicated in red letters in a blue frame. (*a*) Alignment of the N-terminal regions of mammalian TRIF orthologues. (*b*) Alignment of the N-terminal regions of human, chicken and zebra-fish TRIF proteins.

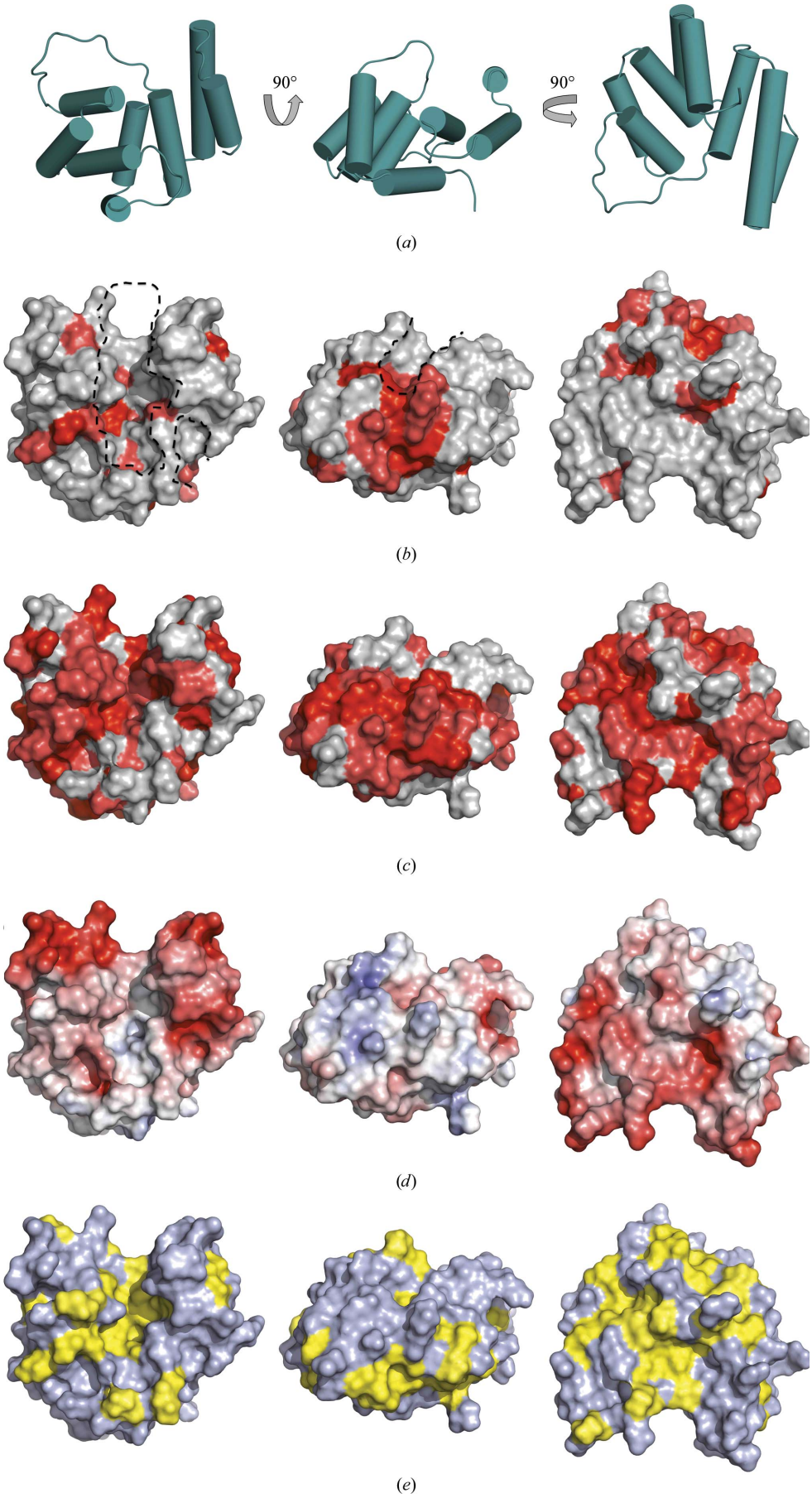

3.4. TRIF-NTD shares structural similarity with IFIT proteins

A search for structurally similar proteins using *DALI* (Holm & Rosenström, 2010) identified significant similarities to tetratricopeptide repeat (TPR) containing proteins, including IFN-induced proteins with tetratricopeptide repeats (IFIT) 1 (*DALI Z* score = 4.4) and 5 (Z = 3.7), the mitochondrial fission protein 1 (Fis1; Z = 3.5), and microtubule interacting and transport (MIT) domain-containing proteins such as the VPS4 ATPase (Z = 3.0) and katanin p60 (Z = 2.6) (Supplementary Fig. S7). TPR is a structural motif that is present in a wide range of proteins and is involved in mediating protein–protein interactions and multiprotein complex assembly (D'Andrea & Regan, 2003). The MIT domain is also involved in protein–protein interactions, and the orientation and the inter-

Figure 5
Surface properties of TRIF-NTD. (*a*) Cylinder representations of TRIF-NTD. (*b*) Conserved TRIF-NTD surface features in human, chicken and zebrafish TRIF proteins. The surface is coloured according to the alignment in Fig. 4(*b*); strictly conserved residues are shown in red and similar residues are shown in light red, while nonconserved residues are coloured grey. The positions of the two largest clefts in TRIF-NTD (calculated with *ProFunc*; Laskowski *et al.*, 2005) are indicated with black dotted lines. (*c*) Conserved surface features between mammalian TRIF-NTD orthologues. The molecules are coloured as in (*b*). (*d*) Surface representations of the molecules in (*b*) and (*c*) with the electrostatic potential (calculated using *APBS*; Baker *et al.*, 2001) mapped onto the surface. Colouring is continuous from blue (potential +5*kT*/e) through white to red (potential −5*kT*/e). (*e*) The surface is coloured according to the hydrophobicity of the side chain, with yellow representing hydrophobic residues and blue representing residues with polar side chains. In (*a*) to (*e*) the molecules in the central and right panels have been rotated relative to the molecule in the left panel.

helical interactions between the two first helices share a similarity to TPR motifs (Scott *et al.*, 2005). The TPR motif is ∼34 amino acids in length and contains two antiparallel helices (helix A and helix B) with eight loosely conserved positions, Trp4, Leu7, Gly8, Tyr11, Ala20, Phe24, Ala27 and Pro32, which mediate the interaction between the two helices (Blatch & Lässle, 1999). In TRIF-NTD, the helix pairs α3–α4 and α6–α7 resemble TPR motifs, with amino acids typical for TPRs found at positions 8, 11, 20, 24 and 27 in the first motif, and 8, 11, 24 and 27 in the second motif (Fig. 3*d*). Not surprisingly, these two helix pairs and their succeeding helices (α5 and α8) are structurally similar to each other, with an r.m.s.d. of 1.4 Å for 42 equivalent C^{α} atoms (Fig. 3*e*). However, the two motifs do not form a continuous repetitive structure in TRIF-NTD.

The TPR-containing IFIT proteins have the highest level of similarity to TRIF-NTD, with overall r.m.s.d. values of 3.2 and 3.4 Å (for 116 and 120 equivalent C^{α} atoms) for IFIT1 and IFIT5, respectively (Fig. 6, Supplementary Fig. S8). Structurally, IFIT proteins can be divided into three TPR-containing regions (Yang *et al.*, 2012; Abbas *et al.*, 2013); in IFIT1 and IFIT5 helices 1–6 form the N-terminal subdomain and helices 7–14 form the central subdomain, while the remaining helices form the C-terminal subdomain (Fig. 6*a*). The first subdomain in TRIF-NTD aligns well with the first five helices of the N-terminal subdomain of IFIT1, IFIT2 and IFIT5 (r.m.s.d. of 2.32 Å for 65 equivalent C^{α} atoms for IFIT1), while the second subdomain in TRIF-NTD aligns well with the three first helices of the central subdomain in IFIT1, IFIT2 and IFIT5 (r.m.s.d. of 2.5 Å for 43 equivalent C^{α} atoms for IFIT1; Figs. 6*b* and 6*c*, Supplementary Fig. S8). The relative positions of the N-terminal and central subdomains in IFIT proteins are also conserved in TRIF-NTD (Fig. 6*c*). In both the TRIF-NTD and the IFIT proteins the first helix of the second subdomain packs against the concave surface of the N-terminal domain, which is reminiscent of the interaction between the TPR-containing protein Fis1 and its ligand (Zhang & Chan, 2007). Interestingly, in the crystal structure of IFIT2 (Yang *et al.*, 2012) the N-terminal subdomain and the three first helices of the central subdomain from two different molecules associate to form a domain-swapped dimer and may explain how IFIT proteins form homo and hetero complexes. However, it is unlikely that TRIF-NTD would form similar domain-swapped dimers as this region of TRIF is not required for homo-oligomerization (Tatematsu *et al.*, 2010).

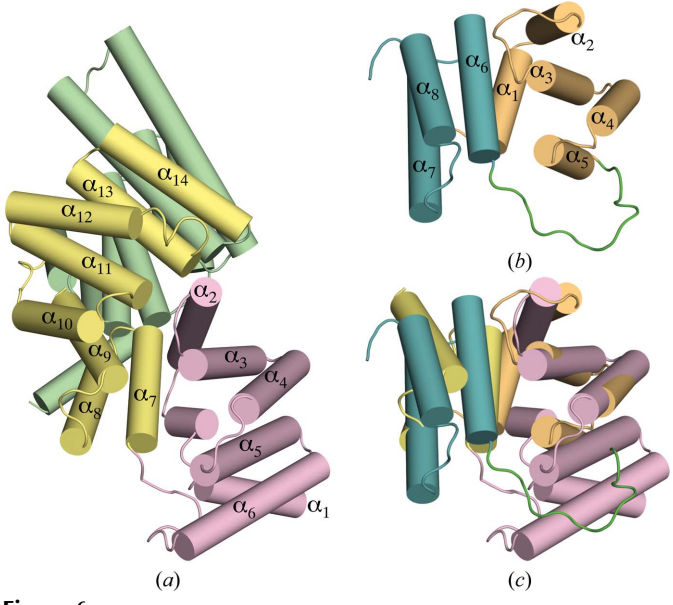

Figure 6
TRIF-NTD shares structural similarity with IFIT proteins. (*a*) Crystal structure of IFIT5 (PDB entry 4hoq; Abbas *et al.*, 2013). The N-terminal, central and C-terminal regions are shown in pink, yellow and green, respectively. (*b*) TRIF-NTD structure in the same orientation as IFIT5 in (*a*). Subdomains 1 and 2 are displayed in orange and teal, respectively. (*c*) Superposition of IFIT5 and TRIF-NTD. Only helices α1–α9 are shown for IFIT5.

IFIT proteins are encoded by a family of genes that are highly induced after stimulation by IFNs, viral infection and PAMP recognition and can inhibit viral infection by suppression of translation initiation and by sequestering of viral proteins or RNA in the cytoplasm (Diamond & Farzan, 2013). IFIT proteins modulate interactions between signalling proteins in the type 1 IFN pathway. IFIT1 has been shown to disrupt the physical interaction between STING (stimulator of IFN genes protein) and TBK1 or MAVS (mitochondrial antiviral-signalling protein) (Li *et al.*, 2009), while IFIT3 can bridge the interaction between MAVS and TBK1, leading to an elevated antiviral response (Liu *et al.*, 2011). The latter interaction requires the N-terminal region of IFIT3, which is structurally similar to TRIF-NTD, and two glutamate residues at the end of the α9 helix of IFIT3 have been shown to be critical for the interaction with TBK1. Although TRIF-NTD is not required for TRIF–TBK1 interaction, the end of the equivalent α7 helix contains residues with similar properties, including two aspartates (Fig. 4*a*), and the surface region also has an electronegative charge. Overall, the similarity between the structures of TRIF-NTD and of the N-terminal region of IFIT proteins may suggest that they have functionally similar roles, which is consistent with the previously proposed regulatory role for TRIF-NTD in TRIF signalling (Tatematsu *et al.*, 2010).

3.5. Identification of possible binding sites in TRIF-NTD involved in TRIF auto-regulation and binding to signalling partners

One of the suggested functions for TRIF-NTD is binding to the TRIF TIR domain as part of the auto-regulatory mechanism (Tatematsu *et al.*, 2010). The amino-acid sequence of TRIF-NTD is highly conserved in mammals, with sequence identities ranging from 63 to 100% (Fig. 4*a*). The equivalent regions in TRIF variants from bird and fish species only share 34–37% and 24–28% identity with human TRIF, respectively, but many of the strictly conserved residues are buried and are critical for stabilizing the structure (Fig. 4*b* and Supplementary Fig. S9), suggesting that they have an analogous fold to human TRIF-NTD. To identify possible binding sites involved in TRIF auto-regulation, we looked for surface regions

present in the structure that exhibited a high degree of sequence conservation among TRIF orthologues. Two programs, *ProFunc* (Laskowski *et al.*, 2005) and *ESPript* (Gouet *et al.*, 2003), were used to consider both sequence and structural information from mammalian TRIF species and diverse TRIF sequences from mammals, birds and fish (Fig. 4). Surface calculations using *ProFunc* identified two major clefts with a cutoff volume of >700 Å^3. The two clefts are located next to each other and may be considered as a continuous surface feature. The largest cleft has a volume of 1500 Å^3 and is localized at the junction between the two helical subdomains (Fig. 5*b*). This cleft has a length of 30 Å and a width of 6–12 Å, which could accommodate a six-to-eight-residue polypeptide chain with extended secondary structure. The side walls of this cleft consist of residues from the α3, α5, α7 and α8 helices and the loop connecting the α5 and α6 helices, whereas the base of the pocket is mostly formed by helix α6, the loop connecting the α2 and α3 helices and the end of the loop connecting the α5 and α6 helices. This cleft has significant sequence conservation within mammals, but not between mammals, birds and fish (Figs. 5*b* and 5*c*), which may suggest that in these two cases the cleft has evolved to accommodate different binding partners or that the binding partner differs substantially between mammals on the one hand and bird and fish species on the other. The most highly conserved residues within the pocket in mammalian TRIF are localized deep in the cleft and include several hydrophobic residues (Leu42, Val69, Val92, Trp94, Ala95 and Leu99; Fig. 5*e*). The walls and regions surrounding the pocket include several conserved polar and charged residues including Gln40, Asp67, Glu87, Glu88, Asp91, Arg132, Glu135 and Glu139 (Fig. 5*d*). Overall, the base of the cleft is highly hydrophobic, while the entry and exit points have a negative charge. The second cleft is significantly smaller than cleft 1 and includes residues from the α2, α6 and α8 helices and the loop connecting the α2 and α3 helices (Fig. 5*b*). Residues Lys29, Leu43, Leu102, Leu103, Glu105 and Glu106, which are conserved or similar in mammals, birds and fish, form the floor and walls of one half of cleft 2 (Fig. 5*b*). These residues are also part of an extended surface patch on the top face of the molecule with high similarity in mammalian, bird and fish TRIF species, suggesting that this region of the TRIF-NTD molecule might also function as an interaction surface (Fig. 5*b*). In addition to the conserved residues in cleft 2, this surface patch consists of residues Ile14, Ala17, Ala18, Lys22, Ile59, Ala104, Lys107, Leu108 and Cys109.

4. Conclusions

In this study, we present the structural and functional characterization of the NTD of the TLR signalling adaptor TRIF. We determined the crystal structure of the protease-resistant TRIF-NTD (residues 1–153) at 2.22 Å resolution by using SAD phasing with an SeMet-labelled protein containing two additional introduced Met residues. The structure shows two helical subdomains connected by a 14-residue linker. The helix pairs resemble TPR-like motifs and the overall fold of TRIF-NTD shares significant structural similarity with the IFIT family of proteins, which are also involved in innate immune signalling. The structure suggests possible surfaces that could mediate the interaction with the TIR domain as part of the proposed auto-regulatory mechanism (Tatematsu *et al.*, 2010) or possibly with unknown interaction partners. Based on the similarities to IFIT proteins and to TPR proteins in general, TRIF-NTD could serve as the sensor domain for an as-yet unknown ligand, with the interaction exposing the binding sites for TBK1, resulting in type 1 IFN signalling. This would also be consistent with the data showing that the deletion of TRIF-NTD leads to increased IFN production and is also similar to mechanisms proposed for PRRs such as NLRs and plant resistance (R) proteins, in which the LRR domain has a dual sensor and auto-regulatory role. Significantly, exogenous TRIF-NTD suppressed the activation of both the IFNβ and NF-κB promoters, providing further evidence for the auto-regulatory role of NTD in TRIF and suggesting that our construct could serve as a therapeutic reagent targeting TLR3- and TLR4-mediated inflammation.

We thank Eugene Valkov, Simon Williams, Rafael Counago, Daniel Ericsson and other members of the Kobe laboratory for help and discussions. This work was supported by the National Health and Medical Research Council (NHMRC grant 1003326 to BK and AM) and the Victorian Government's Operational Support Program. BK is an NHMRC Senior Research Fellow and MJS is an Australian Research Council Future Fellow (FT100100657) and an Honorary NHMRC Senior Research Fellow (APP1003470).

References

Abbas, Y. M., Pichlmair, A., Górna, M. W., Superti-Furga, G. & Nagar, B. (2013). *Nature (London)*, **494**, 60–64.
Adams, P. D., Baker, D., Brunger, A. T., Das, R., DiMaio, F., Read, R. J., Richardson, D. C., Richardson, J. S. & Terwilliger, T. C. (2013). *Annu. Rev. Biophys.* **42**, 265–287.
Akira, S., Uematsu, S. & Takeuchi, O. (2006). *Cell*, **124**, 783–801.
Baker, N. A., Sept, D., Joseph, S., Holst, M. J. & McCammon, J. A. (2001). *Proc. Natl Acad. Sci. USA*, **98**, 10037–10041.
Barton, G. M. & Kagan, J. C. (2009). *Nature Rev. Immunol.* **9**, 535–542.
Blanc, E., Roversi, P., Vonrhein, C., Flensburg, C., Lea, S. M. & Bricogne, G. (2004). *Acta Cryst.* D**60**, 2210–2221.
Blatch, G. L. & Lässle, M. (1999). *Bioessays*, **21**, 932–939.
Bonardi, V., Cherkis, K., Nishimura, M. T. & Dangl, J. L. (2012). *Curr. Opin. Immunol.* **24**, 41–50.
D'Andrea, L. D. & Regan, L. (2003). *Trends Biochem. Sci.* **28**, 655–662.
Das, A. K., Cohen, P. W. & Barford, D. (1998). *EMBO J.* **17**, 1192–1199.
Diamond, M. S. & Farzan, M. (2013). *Nature Rev. Immunol.* **13**, 46–57.
Eisenächer, K. & Krug, A. (2012). *Eur. J. Cell Biol.* **91**, 36–47.
Emsley, P., Lohkamp, B., Scott, W. G. & Cowtan, K. (2010). *Acta Cryst.* D**66**, 486–501.
Fitzgerald, K. A., Rowe, D. C., Barnes, B. J., Caffrey, D. R., Visintin, A., Latz, E., Monks, B., Pitha, P. M. & Golenbock, D. T. (2003). *J. Exp. Med.* **198**, 1043–1055.
Funami, K., Sasai, M., Ohba, Y., Oshiumi, H., Seya, T. & Matsumoto, M. (2007). *J. Immunol.* **179**, 6867–6872.
Funami, K., Sasai, M., Oshiumi, H., Seya, T. & Matsumoto, M. (2008). *J. Biol. Chem.* **283**, 18283–18291.

Gouet, P., Robert, X. & Courcelle, E. (2003). *Nucleic Acids Res.* **31**, 3320–3323.
Han, K.-J., Su, X., Xu, L.-G., Bin, L.-H., Zhang, J. & Shu, H.-B. (2004). *J. Biol. Chem.* **279**, 15652–15661.
Han, K.-J., Yang, Y., Xu, L.-G. & Shu, H.-B. (2010). *J. Biol. Chem.* **285**, 12543–12550.
He, S., Liang, Y., Shao, F. & Wang, X. (2011). *Proc. Natl Acad. Sci. USA*, **108**, 20054–20059.
Holm, L. & Rosenström, P. (2010). *Nucleic Acids Res.* **38**, W545–W549.
Kaiser, W. J. & Offermann, M. K. (2005). *J. Immunol.* **174**, 4942–4952.
Kawai, T. & Akira, S. (2010). *Nature Immunol.* **11**, 373–384.
Kingeter, L. M. & Lin, X. (2012). *Cell. Mol. Immunol.* **9**, 105–112.
Krissinel, E. & Henrick, K. (2007). *J. Mol. Biol.* **372**, 774–797.
Langer, G., Cohen, S. X., Lamzin, V. S. & Perrakis, A. (2008). *Nature Protoc.* **3**, 1171–1179.
Larkin, M. A., Blackshields, G., Brown, N. P., Chenna, R., McGettigan, P. A., McWilliam, H., Valentin, F., Wallace, I. M., Wilm, A., Lopez, R., Thompson, J. D., Gibson, T. J. & Higgins, D. G. (2007). *Bioinformatics*, **23**, 2947–2948.
Laskowski, R. A., Watson, J. D. & Thornton, J. M. (2005). *Nucleic Acids Res.* **33**, W89–W93.
Li, Y., Li, C., Xue, P., Zhong, B., Mao, A.-P., Ran, Y., Chen, H., Wang, Y.-Y., Yang, F. & Shu, H.-B. (2009). *Proc. Natl Acad. Sci. USA*, **106**, 7945–7950.
Liu, X.-Y., Chen, W., Wei, B., Shan, Y.-F. & Wang, C. (2011). *J. Immunol.* **187**, 2559–2568.
McCoy, A. J., Grosse-Kunstleve, R. W., Adams, P. D., Winn, M. D., Storoni, L. C. & Read, R. J. (2007). *J. Appl. Cryst.* **40**, 658–674.
Meylan, E., Burns, K., Hofmann, K., Blancheteau, V., Martinon, F., Kelliher, M. & Tschopp, J. (2004). *Nature Immunol.* **5**, 503–507.
O'Neill, L. A. & Bowie, A. G. (2007). *Nature Rev. Immunol.* **7**, 353–364.
Oshiumi, H., Matsumoto, M., Funami, K., Akazawa, T. & Seya, T. (2003). *Nature Immunol.* **4**, 161–167.
Oshiumi, H., Sasai, M., Shida, K., Fujita, T., Matsumoto, M. & Seya, T. (2003). *J. Biol. Chem.* **278**, 49751–49762.
Sasai, M., Tatematsu, M., Oshiumi, H., Funami, K., Matsumoto, M., Hatakeyama, S. & Seya, T. (2010). *Mol. Immunol.* **47**, 1283–1291.
Scott, A., Gaspar, J., Stuchell-Brereton, M. D., Alam, S. L., Skalicky, J. J. & Sundquist, W. I. (2005). *Proc. Natl Acad. Sci. USA*, **102**, 13813–13818.
Stivala, A., Wybrow, M., Wirth, A., Whisstock, J. C. & Stuckey, P. J. (2011). *Bioinformatics*, **27**, 3315–3316.
Tatematsu, M., Ishii, A., Oshiumi, H., Horiuchi, M., Inagaki, F., Seya, T. & Matsumoto, M. (2010). *J. Biol. Chem.* **285**, 20128–20136.
Ullah, M. O., Ve, T., Dkhar, J., Alaidarous, M., Ericsson, D. J., Sweet, M. J., Mansell, A. & Kobe, B. (2013). *Acta Cryst.* F**69**, 766–770.
Unneberg, P., Merelo, J. J., Chacón, P. & Morán, F. (2001). *Proteins*, **42**, 460–470.
Unni, S., Huang, Y., Hanson, R. M., Tobias, M., Krishnan, S., Li, W. W., Nielsen, J. E. & Baker, N. A. (2011). *J. Comput. Chem.* **32**, 1488–1491.
Ve, T., Gay, N. J., Mansell, A., Kobe, B. & Kellie, S. (2012). *Curr. Drug Targets*, **13**, 1360–1374.
Werts, C., Girardin, S. E. & Philpott, D. J. (2006). *Cell Death Differ.* **13**, 798–815.
Wiedemann, C., Bellstedt, P. & Görlach, M. (2013). *Bioinformatics*, **29**, 1750–1757.
Winn, M. D. *et al.* (2011). *Acta Cryst.* D**67**, 235–242.
Yamamoto, M., Sato, S., Hemmi, H., Hoshino, K., Kaisho, T., Sanjo, H., Takeuchi, O., Sugiyama, M., Okabe, M., Takeda, K. & Akira, S. (2003). *Science*, **301**, 640–643.
Yang, Z., Liang, H., Zhou, Q., Li, Y., Chen, H., Ye, W., Chen, D., Fleming, J., Shu, H. & Liu, Y. (2012). *Cell Res.* **22**, 1328–1338.
Zhang, Y. & Chan, D. C. (2007). *Proc. Natl Acad. Sci. USA*, **104**, 18526–18530.